Tracking Quantum Coherence in Polariton Condensates with Time-Resolved Tomography

Carolin Lüders,[1,*] Matthias Pukrop,[2] Franziska Barkhausen,[2] Elena Rozas,[1] Christian Schneider,[3] Sven Höfling,[4] Jan Sperling,[5,†] Stefan Schumacher,[2,6] and Marc Aßmann[1]

[1]*Experimentelle Physik 2, Technische Universität Dortmund, D-44221 Dortmund, Germany*
[2]*Department of Physics and Center for Optoelectronics and Photonics Paderborn (CeOPP), Universität Paderborn, 33098 Paderborn, Germany*
[3]*Institute of Physics, University of Oldenburg, D-26129 Oldenburg, Germany*
[4]*Technische Physik, Physikalisches Institut and Würzburg-Dresden Cluster of Excellence ct.qmat, Universität Würzburg, 97074 Würzburg, Germany*
[5]*Theoretical Quantum Science, Institute for Photonic Quantum Systems (PhoQS), Paderborn University, Warburger Straße 100, 33098 Paderborn, Germany*
[6]*Wyant College of Optical Sciences, University of Arizona, Tucson, Arizona 85721, USA*

(Received 15 September 2022; accepted 21 February 2023; published 13 March 2023)

Long-term quantum coherence constitutes one of the main challenges when engineering quantum devices. However, easily accessible means to quantify complex decoherence mechanisms are not readily available, nor are sufficiently stable systems. We harness novel phase-space methods—expressed through non-Gaussian convolutions of highly singular Glauber-Sudarshan quasiprobabilities—to dynamically monitor quantum coherence in polariton condensates with significantly enhanced coherence times. Via intensity- and time-resolved reconstructions of such phase-space functions from homodyne detection data, we probe the systems' resourcefulness for quantum information processing up to the nanosecond regime. Our experimental findings are confirmed through numerical simulations, for which we develop an approach that renders established algorithms compatible with our methodology. In contrast to commonly applied phase-space functions, our distributions can be directly sampled from measured data, including uncertainties, and yield a simple operational measure of quantum coherence via the distribution's variance in phase. Therefore, we present a broadly applicable framework and a platform to explore time-dependent quantum phenomena and resources.

DOI: 10.1103/PhysRevLett.130.113601

Introduction.—Applications in quantum information science require stable quantum superpositions as a key resource. Therefore, a great deal of effort is dedicated to quantifying quantum coherence [1–6]. Beyond assessing the amount of useful quantumness, however, the evolution of quantum coherence is, at least, equally important to actually processing information in quantum algorithms [7–9]. Furthermore, quantum coherence, providing a single number, does not yield an exhaustive quantum state description, generally not allowing for proposing schemes to access particular quantum resources. In this Letter, we overcome the challenging problem of studying dynamic quantum coherence, while also providing a comprehensive and accessible quantum state description.

In quantum information science, quantum coherence is based on a set of computational and orthonormal basis states [3], which are number states $|n\rangle$ in our study. Exceeding incoherent mixtures—i.e., diagonal $\hat{\rho} = \sum_n p_n |n\rangle\langle n|$—results in quantum superpositions—e.g., $\hat{\rho} = |\psi\rangle\langle\psi|$ with $|\psi\rangle = \sum_n \psi_n |n\rangle$—that form the foundation of quantum algorithms [5], such as quantum teleportation [10], Shor's factorization [11], quantum key distribution [12], etc. It was shown in Ref. [13] that, in optical and semiconductor systems, this operational quantification of quantum coherence for practical quantum protocols is distinctively different from commonly applied notions of nonclassicality and macroscopic coherence as characterized through negativities in phase-space functions [14] and determined by correlation functions [15], respectively.

Polaritons in semiconductor microcavities present a so-far untapped resource of quantum coherence [13]. Polaritons—i.e., hybrid light-matter quasiparticles—arise from the strong coupling between the cavity photons and the quantum well excitons. Under nonresonant excitation, polaritons can spontaneously form a macroscopic coherent condensate [16,17]. The buildup of quantum coherence was demonstrated across the condensation threshold, while an incoherent thermal behavior was observed below threshold [13]. Nevertheless, the evolution and other vital information about the produced states were inaccessible, posing open problems to date. Generally, the dynamics of

polariton condensates has been studied in previous experiments, mainly by measuring the field correlation $g^{(1)}$ using Michelson and Mach-Zehnder interferometry [18–21], and the second-order correlation $g^{(2)}$ via Hanbury Brown–Twiss interferometry [22,23]. But such correlation functions do not yield information about quantum coherence in the quantum-informational sense [13], which depends on superimposing computational basis states [3].

In this contribution, we establish an easily applicable method for analyzing quantum coherence via time-resolved quantum tomography. To this end, we adopt advanced phase-space functions, labeled as P_Ω, for tracking quantum coherence produced by a polariton microcavity system. The phase variance of P_Ω allows us to quantify quantum coherence, and we demonstrate that P_Ω can be directly sampled from our data using pattern functions. Exceptionally long coherence times—up to 1390 ps—are experimentally observed. This is further supported by microscopic simulations, advancing the truncated Wigner approximation [24,25] to phase-space methods based on P_Ω. This renders it possible to reconstruct P_Ω, compare the numerical results to our experiment, reveal important parameter dynamics, and relate our measurements to key aspects of the underlying physical system.

Regularized phase-space functions P_Ω.—Phase-space distributions based on coherent states $|\alpha\rangle$ are useful for determining typical nonclassical effects, and they provide a full state description [14]. However, information-based quantum coherence relies on orthogonal states as the classical reference, such as number states $|n\rangle$, but not coherent states. Moreover, the fundamental Glauber-Sudarshan phase-space distribution P [26,27], where $\hat{\rho} = \int d^2\alpha P(\alpha)|\alpha\rangle\langle\alpha|$, can exhibit an exponential order of singularities [28]. Thus, convolution-based regularizations were developed [29,30]:

$$P_\Omega(\alpha) = \int d^2\gamma \Omega(\gamma - \alpha) P(\gamma). \tag{1}$$

For instance, the seminal Husimi Q function and the Wigner function are obtained when Ω is a Gaussian kernel. Still, the reconstruction of such common phase-space functions can be rather challenging, including ill-posed inversions [31,32], diverging pattern functions [33,34], and demanding maximum-likelihood estimations [35–37].

For optical scenarios, a regularization of P distributions has been proposed to characterize nonclassical light by utilizing non-Gaussian kernels [38]; see Refs. [39,40] for recent experiments. While phase-space representations have been applied to semiconductor systems in pioneering papers [41–43], to date, this modern non-Gaussian approach to phase-space representations has not been exploited to analyze quantum coherence properties of semiconductors and their dynamics.

Here, we use the non-Gaussian and phase-invariant kernel

$$\Omega(\gamma) = \left[\frac{J_1(2R|\gamma|)}{\sqrt{\pi}|\gamma|}\right]^2, \tag{2}$$

with J_1 denoting the first Bessel function of the first kind and $R > 0$ being an adjustable width parameter. Remarkably, the regularized function P_Ω can be directly obtained from data [44], with $P_\Omega(\alpha) \approx \sum_i w_i f_\Omega(\alpha, x_i; \varphi_i)$, circumventing all aforementioned reconstruction problems. In the formula, (x_i, φ_i) is the ith quadrature measurement from balanced homodyne detection, w_i's are weights, and f_Ω's are pattern functions; see the Supplemental Material [45] for details.

Incoherent contributions to the density operator—e.g., $|n\rangle\langle n|$—relate to phase-independent parts of P_Ω, depending on the amplitude $|\alpha|$ only. Conversely, the distribution of the phase $\phi = \arg\alpha$ is directly connected to off-diagonal density operator terms, $|n\rangle\langle m|$ for $m \neq n$, thus determining quantum coherence [13,45]. Therefore, we here introduce the width of P_Ω in phase as an operational measure of quantum coherence. Specifically, the circular variance [61]

$$\mathrm{Var}(\phi) = 1 - |\langle r\rangle|, \quad \text{with} \quad \langle r\rangle = \int d^2\alpha P_\Omega(\alpha)\frac{\alpha}{|\alpha|} \tag{3}$$

takes the maximal value 1 for a fully phase-randomized—i.e., incoherent—state; a narrow phase distribution—hence, a low circular variance—is obtained for strongly off-diagonal density operators, verifying a high degree of quantum coherence [45]. Therefore, the evolution of this circular variance of P_Ω monitors the dynamics of quantum coherence.

Experimental time-resolved tomography.—Our system is a GaAs polariton microcavity [13,45,46]. The sample is held in a cryostat at 10 K and is excited nonresonantly at the first minimum of the stop band, with a linearly polarized continuous-wave laser. A nonresonant excitation prevents the system from inheriting coherence from the pump [47,62].

For our time-resolved tomography, the sample emission is divided into three homodyne detection channels (see Fig. 1). Two channels provide a proxy measurement of a Husimi function [13,48], and the third one acts as a target arm [49]. Between the target and proxy, a temporal offset τ is controlled via a delay line. An annulus-shaped region of $Q(q_{ps}, p_{ps})$, specified by radius s and thickness w, selects specific intensities. For data in that region, we process the quadrature values q from the target. Besides this, we reconstruct the relative phase φ between the local oscillator (LO) and signal in the target channel by adding the relative phase of the two selection channels, $\varphi_{ps} = \arctan(p_{ps}/q_{ps})$, to the relative phase $\Delta\varphi$ between the LOs in the proxy and target channels. Then, the values (q, φ) are fed into the

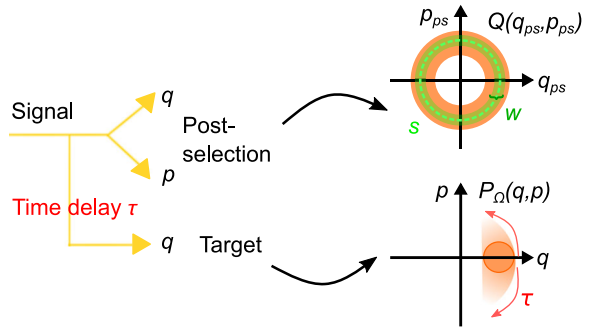

FIG. 1. Experimental concept as conditional intensity spectroscopy. The signal is split into three homodyne detection channels. Two are used for intensity selection, delivering field quadratures (q_{ps}, p_{ps}) of a Husimi function $Q(\alpha_{ps})$, with $\alpha_{ps} = q_{ps} + ip_{ps}$. Thereby, a specific region with radius s and width w is chosen, fixing the signal's mean intensity and its uncertainty. The third quadrature is the target channel for quadratures q. Together with the corresponding phases, this allows us to directly sample P_Ω. The time delay τ determines the elapsed time of the system's evolution.

previously described reconstruction scheme. This yields P_Ω as a function of the variable time delay τ, providing information resolved for each selected intensity region beyond other approaches that average over intensities.

In homodyne detection, one measures the overlap of signal and LO, resulting in a mode selectivity. This allows us to track the evolution of selected signal modes separately. Here, our LO is aligned to the most dominant linear polarization mode in the emission. The LO's wavelength is resonant to the most intense zero-momentum ground-state mode of the polariton emission. The LO has a spectral full width at half maximum (FWHM) of 1.9 nm, a pulse duration of 460 fs, and a FWHM in k space of 1.3 μm^{-1}, centered at $k = 0$.

Experimental results.—Figure 2 (right column) exemplifies reconstructed P_Ω functions for the highest excitation power $P_{exc} = 1.7P_{thr}$ [63] for three different time delays τ. The phase diffuses with increasing τ, resulting in a broadening of the angular distribution. Simultaneously, the mean amplitude of P_Ω relaxes towards a steady-state value.

To resolve the mean amplitude and the circular variance as functions of the selected intensity s and time delays τ, $\langle|\alpha|\rangle$ and $\mathrm{Var}(\phi)$ are derived from reconstructed $P_\Omega(\alpha)$ via Eq. (3) and $\langle|\alpha|\rangle = \int d^2\alpha P_\Omega(\alpha)|\alpha|$, using a discretized set of points $\alpha = q + ip$. The behavior of both quantities is plotted in Figs. 2(a) and 2(b) for $P_{exc} = 1.7P_{thr}$, while $w = 0.6$ is kept constant. Lines depict an exponential fit, empirically yielding the best results compared to Gaussian and power-law fits [45]. $\mathrm{Var}(\phi)$ in Fig. 2(a) has its minimum around $\tau = 0$, the smallest value being 0.14 for the highest selected intensity, $s = 11$. This minimum increases for smaller s because of the phase-photon number uncertainty relation [45]. For increasing delays, the circular

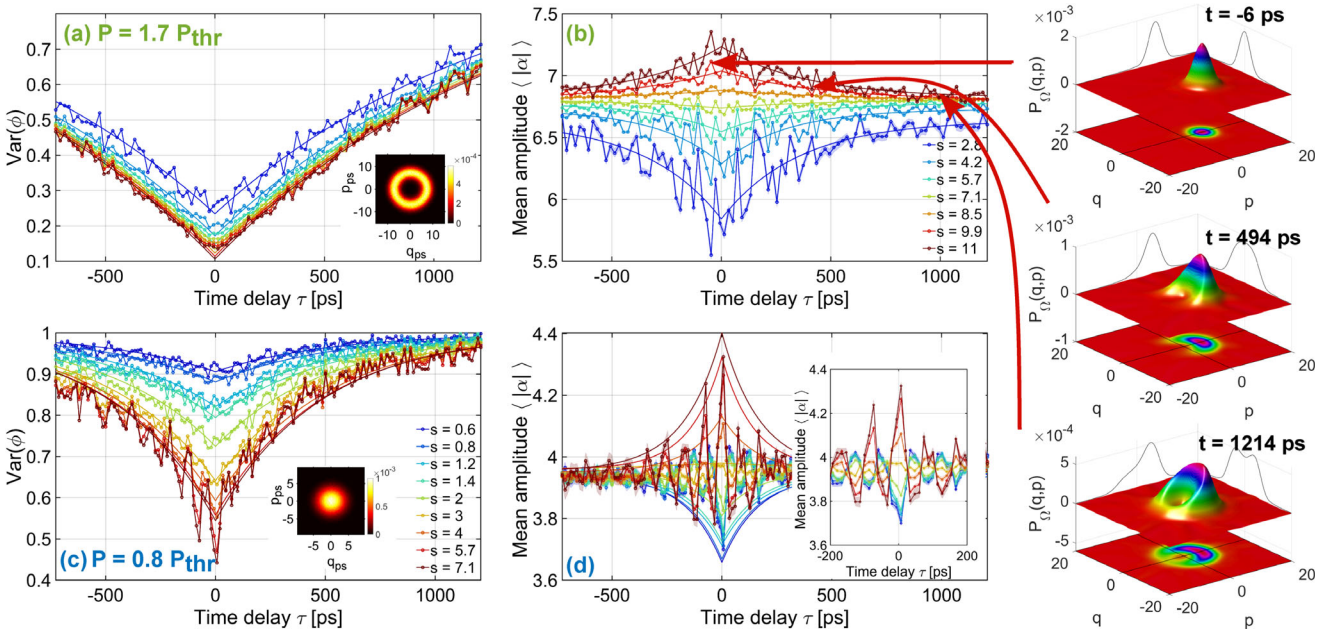

FIG. 2. Temporal behavior of the mean amplitude $\langle|\alpha|\rangle$ and the circular phase variance $\mathrm{Var}(\phi)$ of reconstructed P_Ω, depending on the selected intensity radius s. A shaded area around the curves corresponds to a 1-standard-deviation error margin, directly derived from P_Ω's uncertainty, but is mostly not visible. Lines depict exponential fits. Plots (a) and (b) are for $P_{exc} = 1.7P_{thr}$. The width w of the selected phase-space region is 0.57. Plots (c) and (d) are for $P_{exc} = 0.8P_{thr}$. The width w is 0.1, except for the two highest radii s, where $w = 0.57$. Insets in (a) and (c) show the Husimi functions from which the radius s is selected, cf. Fig. 1. The inset in (d) displays a zoom of the region $\tau \approx 0$, revealing an oscillation of the mean amplitude. The right column exemplifies three P_Ω for $P_{exc} = 1.7P_{thr}$ and a selected radius $s = 9.9$ at time delays $\tau = -6$ ps (top), $\tau = 494$ ps (middle), and $\tau = 1214$ ps (bottom).

variance increases but does not arrive at a uniform distribution [i.e., $\mathrm{Var}(\phi) = 1$], even for the longest delay $\tau = 1214$ ps. By contrast, the mean amplitude $\langle|\alpha|\rangle$ in Fig. 2(b) relaxes almost completely toward the steady-state value, thus decaying faster than the quantum phase.

Figures 2(c) and 2(d) show the results for a lower excitation power, $P_{\mathrm{exc}} = 0.8P_{\mathrm{thr}}$. Here, the phase variance increases faster and reaches almost 1, describing full phase decoherence. Meanwhile, the mean amplitude rapidly decays toward the steady-state value. Our method also reveals an oscillation around the stationary value, with a frequency of 12.5 GHz. (This can be seen for $P_{\mathrm{exc}} = P_{\mathrm{thr}}$ as well, but not for higher powers.) We attribute this effect to mode competition between modes of orthogonal linear polarizations [45]. Such a bistable regime of two cross-linear polarizations and oscillatory behavior has also been proposed in Ref. [64]. But modulations of the spatial density of the polariton condensate—e.g., breathing modes—can also lie in this frequency range [65].

In addition, we estimate decay times τ_c by fitting the temporal dependence of $\langle|\alpha|\rangle$ and $\mathrm{Var}(\phi)$ to exponential functions, $a\exp(-\tau/\tau_c) + d$. In Figs. 3(a) and 3(b), this decay time is plotted versus the selected intensity radius s for different excitation powers. For $\langle|\alpha|\rangle$, there is no significant dependence on s. For $\mathrm{Var}(\phi)$, there is a tendency for states with higher s to have a larger decay time for higher excitation powers, whereas the opposite trend appears for lower powers. This might be explained

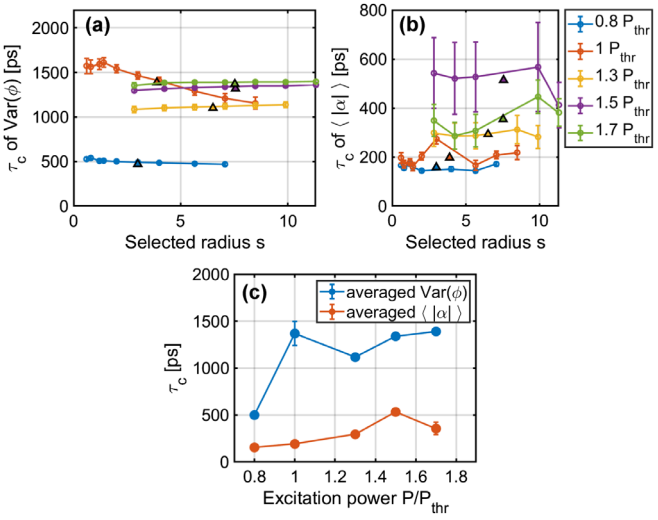

FIG. 3. Decay times (a) τ_c of $\mathrm{Var}(\phi)$ and (b) of the mean amplitude $\langle|\alpha|\rangle$ versus the selected radius s for different excitation powers. Connecting lines are guides for the eye. Triangles indicate the mean radius averaged over the Husimi distribution—i.e., the stationary state. For the amplitude decay times, s values too close to the mean radius are discarded, as fits are error prone due to the flat curve shape in those cases. (c) Decay time τ_c, averaged over the radii s, versus excitation power. For the average, the decay time for each radius has been weighted by the number of data points.

with a lower stability of the system for lower powers, and thus faster relaxation upon perturbations. At $P_{\mathrm{exc}} = P_{\mathrm{thr}}$, the phase decay time is exceptionally long. At this transition between the thermal and coherent states, the system is least affected by heating, interaction with the reservoir, and polariton-polariton interactions, which become relevant decoherence mechanisms at higher excitation powers.

In Fig. 3(c), the decay times are averaged over s and plotted versus P_{exc}. Clearly, the amplitude has a shorter decay time than the phase. Notably, the mean phase coherence time is exceptionally long, between 520 ps and 1390 ps. In earlier studies, values around 100 ps were reported by employing a noise-free single-mode excitation laser [19] and a spatially confined cavity, favoring single-mode emission [21,66]. By condensate trapping with a patterned pump, diminishing reservoir interactions, nanosecond coherence times were demonstrated [18,20,23]. Top-hat-shaped pump lasers, causing less spread of the condensate in k space, led to coherence times of up to 90 ps [18]. However, most of these studies reported a Gaussian shape of $g^{(1)}(\tau)$, especially for higher excitation powers [21,66], suggesting inhomogeneous signal broadening. We, however, attribute our long coherence times to a combination of using a single-mode excitation laser with a relatively large beam diameter, leading to a small spread in k space and less reservoir density, as well as filtering our signal with the LO to remove inhomogeneous broadening.

Simulation.—We also carried out theoretical simulations utilizing a stochastic Gross-Pitaevskii model, based on the truncated Wigner approximation [24,25]. This method was successfully employed to study coherence properties of condensates [13,50,67,68]. Similarly to the experiment, the phase variance is dynamically tracked to probe the decay of quantum coherence. We initialize the system as a displaced thermal state that then evolves. The mean displacement and the standard deviation of the initial distribution are determined through the steady-state values for mean polariton numbers and quantum coherences [45].

Importantly, we employ a convolution-deconvolution approach to derive a relation between our P_Ω function and the Wigner function that unifies existing simulations with our method [45]. While the deconvolution part from the Wigner function to the P distribution would diverge, we find that the following convolution with our non-Gaussian Ω in Eq. (2) eventually yields well-defined expressions, being paramount for numerical analyses.

Figure 4 shows the numerical results for the time-dependent circular variance and the correspondingly fitted coherence time τ_c of the zero-momentum condensate mode for different excitation powers. τ_c increases significantly around the threshold excitation power P_{thr} and reaches values from 0.5 ns to 1.5 ns, being comparable to the experiment until about $1.5P_{\mathrm{thr}}$. Decoherence can be attributed to the nonlinear part of the effective potential, caused

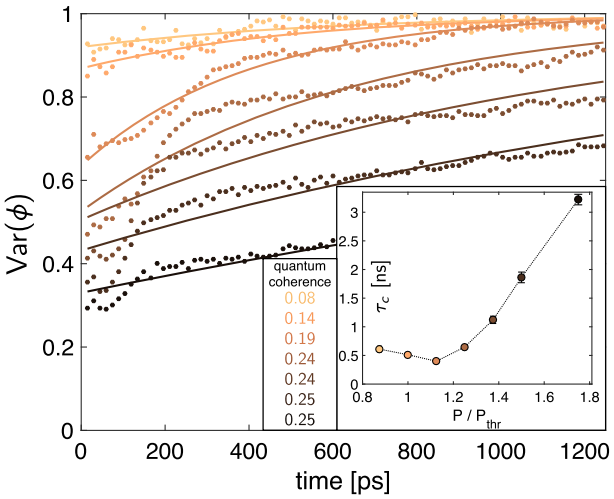

FIG. 4. Numerical results. Circular variance $\mathrm{Var}(\phi)$ from P_Ω for the $k = 0$ condensate mode as a function of time for different excitation powers. Lines are the fitted exponential curves, color-coded to the excitation powers as defined in the inset; the inset shows the fitted coherence times τ_c as a function of the excitation power, with error margins of 1 standard deviation. Additionally, the values of quantum coherence are given.

by interactions of the polaritons with themselves and the reservoir. Density fluctuations, in turn, lead to frequency fluctuations in the condensate mode that constitute an intrinsic decoherence mechanism [19], which is particularly relevant for lower polariton densities near the threshold. Unlike the experiment, however, the coherence time in the simulation does not saturate, but continues to increase beyond $1.5P_{\mathrm{thr}}$. This is due to the lack of decoherence mechanisms in the numerical model, which become experimentally important at higher excitation powers—e.g., temperature effects due to sample heating and higher-order scattering processes, as discussed above.

We further find that τ_c decreases with increasing interaction strength g_c and with decreasing condensate-reservoir interaction g_r. These trends are an effect of the effective potential that causes the decoherence in the numerical model. Up to first order, the nonlinear part of the effective potential reads $V_{\mathrm{nl}} = g_c[1 - P^*_{\mathrm{pump}}(g_r\gamma_c)/(g_c\gamma_r)]|\psi|^2$ [69], with $P^*_{\mathrm{pump}} \equiv P_{\mathrm{pump}}R_r/(\gamma_c\gamma_r)$, revealing the observed parameter trends. Coherence times also depend on the spatial pump profile, altering the spectral shape of the emission [51]. Moreover, we find that, in the presence of a realistic static disorder potential, the condensate emission is slightly shifted to finite k values, but the coherence times of the maximum-intensity mode remain similar to the values without disorder.

Conclusion.—By combining quantum dynamics, modern phase-space methods, and coherence quantifiers of quantum-technological resourcefulness, we explored the evolution of polariton condensates. We implemented a phase-space-based approach to access quantum coherence via circular variances and to characterize the state, while also overcoming limitations of other phase-space reconstruction techniques. And we devised a numerical approach that renders state-of-the-art simulations compatible to our methodology. Thereby, an advanced framework to dynamically track the quantum-informational resourcefulness of polariton condensates is established and implemented.

We employed multichannel homodyne detection to directly reconstruct advanced phase-space representations. While homodyne detection allows one to selectively filter on one mode for measurement, our conditional spectroscopy further enabled us to analyze the dynamics of the state as a function of the initial intensity. We thereby observed long decay times of quantum coherence on the order of 1 ns, agreeing well with our simulations.

Combining the here-developed strategies with our multichannel detection [49] and generalized multimode phase-space methods [70] further paves the way for future investigations, such as the interplay between different condensate modes to explore mode competition [23] and the dynamical characterization of multimode quantum correlations [40]. Furthermore, our approach can also advance the study of other quantum systems beyond the specific scenario explored here, such as trapped ions [71] and ensembles of atoms [72].

The authors acknowledge funding through the Deutsche Forschungsgemeinschaft (DFG, German Research Foundation) via the transregional collaborative research center TRR 142 (Projects A04 and C10, Grant No. 231447078). A grant for computing time at the Paderborn Center for Parallel Computing (PC^2) is gratefully acknowledged.

*carolin.lueders@tu-dortmund.de
†jan.sperling@upb.de

[1] A. Streltsov, G. Adesso, and M. B. Plenio, Colloquium: Quantum coherence as a resource, Rev. Mod. Phys. **89**, 041003 (2017).
[2] E. Chitambar and G. Gour, Quantum resource theories, Rev. Mod. Phys. **91**, 025001 (2019).
[3] T. Baumgratz, M. Cramer, and M. B. Plenio, Quantifying Coherence, Phys. Rev. Lett. **113**, 140401 (2014).
[4] F. Levi and F. Mintert, A quantitative theory of coherent delocalization, New J. Phys. **16**, 033007 (2014).
[5] J. Sperling and W. Vogel, Convex ordering and quantification of quantumness, Phys. Scr. **90**, 074024 (2015).
[6] A. Winter and D. Yang, Operational Resource Theory of Coherence, Phys. Rev. Lett. **116**, 120404 (2016).
[7] M. A. Nielsen and I. L. Chuang, *Quantum Computation and Quantum Information*, 10th ed. (Cambridge University Press, Cambridge, England, 2010).
[8] J. P. Dowling and J. G. Milburn, Quantum technology: The second quantum revolution, Phil. Trans. R. Soc. A **361**, 1655 (2003).

[9] I. H. Deutsch, Harnessing the power of the second quantum revolution, PRX Quantum **1**, 020101 (2020).
[10] C. H. Bennett, G. Brassard, C. Crépeau, R. Jozsa, A. Peres, and W. K. Wootters, Teleporting an Unknown Quantum State via Dual Classical and Einstein-Podolsky-Rosen Channels, Phys. Rev. Lett. **70**, 1895 (1993).
[11] P. W. Shor, Polynomial-time algorithms for prime factorization and discrete logarithms on a quantum computer, SIAM J. Sci. Statist. Comput. **26**, 1484 (1997).
[12] C. H. Bennett and G. Brassard, Quantum cryptography: Public key distribution and coin tossing, Theor. Comput. Sci. **560** (Part 1), 7 (2014).
[13] C. Lüders, M. Pukrop, E. Rozas, C. Schneider, S. Höfling, J. Sperling, S. Schumacher, and M. Aßmann, Quantifying quantum coherence in polariton condensates, PRX Quantum **2**, 030320 (2021).
[14] J. Sperling and W. Vogel, Quasiprobability distributions for quantum-optical coherence and beyond, Phys. Scr. **95**, 034007 (2020).
[15] E. V. Shchukin and W. Vogel, Nonclassical moments and their measurement, Phys. Rev. A **72**, 043808 (2005).
[16] I. Carusotto and C. Ciuti, Quantum fluids of light, Rev. Mod. Phys. **85**, 299 (2013).
[17] H. Deng, H. Haug, and Y. Yamamoto, Exciton-polariton Bose-Einstein condensation, Rev. Mod. Phys. **82**, 1489 (2010).
[18] A. Askitopoulos, L. Pickup, S. Alyatkin, A. Zasedatelev, K. G. Lagoudakis, W. Langbein, and P. G. Lagoudakis, Giant increase of temporal coherence in optically trapped polariton condensate, arXiv:1911.08981.
[19] A. P. D. Love, D. N. Krizhanovskii, D. M. Whittaker, R. Bouchekioua, D. Sanvitto, S. Al Rizeiqi, R. Bradley, M. S. Skolnick, P. R. Eastham, R. André, and L. S. Dang, Intrinsic Decoherence Mechanisms in the Microcavity Polariton Condensate, Phys. Rev. Lett. **101**, 067404 (2008).
[20] K. Orfanakis, A. F. Tzortzakakis, D. Petrosyan, P. G. Savvidis, and H. Ohadi, Ultralong temporal coherence in optically trapped exciton-polariton condensates, Phys. Rev. B **103**, 235313 (2021).
[21] S. Kim, B. Zhang, Z. Wang, J. Fischer, S. Brodbeck, M. Kamp, C. Schneider, S. Höfling, and H. Deng, Coherent Polariton Laser, Phys. Rev. X **6**, 011026 (2016).
[22] M. Klaas, H. Flayac, M. Amthor, I. G. Savenko, S. Brodbeck, T. Ala-Nissila, S. Klembt, C. Schneider, and S. Höfling, Evolution of Temporal Coherence in Confined Exciton-Polariton Condensates, Phys. Rev. Lett. **120**, 017401 (2018).
[23] S. Baryshev, A. Zasedatelev, H. Sigurdsson, I. Gnusov, J. D. Töpfer, A. Askitopoulos, and P. G. Lagoudakis, Engineering Photon Statistics in a Spinor Polariton Condensate, Phys. Rev. Lett. **128**, 087402 (2022).
[24] A. Sinatra, C. Lobo, and Y. Castin, The truncated Wigner method for Bose-condensed gases: Limits of validity and applications, J. Phys. B **35**, 3599 (2002).
[25] P. B. Blakie, A. S. Bradley, M. J. Davis, R. J. Ballagh, and C. W. Gardiner, Dynamics and statistical mechanics of ultracold Bose gases using c-field techniques, Adv. Phys. **57**, 363 (2008).
[26] R. J. Glauber, Coherent and incoherent states of the radiation field, Phys. Rev. **131**, 2766 (1963).
[27] E. C. G. Sudarshan, Equivalence of Semiclassical and Quantum Mechanical Descriptions of Statistical Light Beams, Phys. Rev. Lett. **10**, 277 (1963).
[28] J. Sperling, Characterizing maximally singular phase-space distributions, Phys. Rev. A **94**, 013814 (2016).
[29] K. E. Cahill and R. J. Glauber, Density operators and quasiprobability distributions, Phys. Rev. **177**, 1882 (1969).
[30] G. S. Agarwal and E. Wolf, Calculus for functions of noncommuting operators and general phase-space methods in quantum mechanics. II. Quantum mechanics in phase space, Phys. Rev. D **2**, 2187 (1970).
[31] S. M. Tan, An inverse problem approach to optical homodyne tomography, J. Mod. Opt. **44**, 2233 (1997).
[32] V. N. Starkov, A. A. Semenov, and H. V. Gomonay, Numerical reconstruction of photon-number statistics from photocounting statistics: Regularization of an ill-posed problem, Phys. Rev. A **80**, 013813 (2009).
[33] T. Richter, Pattern functions used in tomographic reconstruction of photon statistics revisited, Phys. Lett. A **211**, 327 (1996).
[34] U. Leonhard, M. Munroe, T. Kiss, T. Richter, and M. G. Raymer, Sampling of photon statistics and density matrix using homodyne detection, Opt. Commun. **127**, 144 (1996).
[35] Z. Hradil, Quantum-state estimation, Phys. Rev. A **55**, R1561(R) (1997).
[36] A. I. Lvovsky, Iterative maximum-likelihood reconstruction in quantum homodyne tomography, J. Opt. B **6**, S556 (2004).
[37] R. Kosut, I. A. Walmsley, and H. Rabitz, Optimal Experiment Design for Quantum State and Process Tomography and Hamiltonian Parameter Estimation, arXiv:quant-ph/0411093.
[38] T. Kiesel and W. Vogel, Nonclassicality filters and quasiprobabilities, Phys. Rev. A **82**, 032107 (2010).
[39] B. Kühn, W. Vogel, V. Thiel, S. Merkouche, and B. J. Smith, Gaussian versus Non-Gaussian Filtering of Phase-Insensitive Nonclassicality, Phys. Rev. Lett. **126**, 173603 (2021).
[40] S. Köhnke, E. Agudelo, M. Schünemann, O. Schlettwein, W. Vogel, J. Sperling, and B. Hage, Quantum Correlations beyond Entanglement and Discord, Phys. Rev. Lett. **126**, 170404 (2021).
[41] M. Kira and S. W. Koch, Cluster-expansion representation in quantum optics, Phys. Rev. A **78**, 022102 (2008).
[42] M. Kira, S. W. Koch, R. P. Smith, A. E. Hunter, and S. T. Cundiff, Quantum spectroscopy with Schrödinger cat states, Nat. Phys. **7**, 799 (2011).
[43] A. E. Almand-Hunter, H. Li, S. T. Cundiff, M. Mootz, S. Kira, and S. W. Koch, Quantum droplets of electrons and holes, Nature (London) **506**, 471 (2014).
[44] T. Kiesel, W. Vogel, B. Hage, and R. Schnabel, Direct Sampling of Negative Quasiprobabilities of a Squeezed State, Phys. Rev. Lett. **107**, 113604 (2011).
[45] See Supplemental Material at http://link.aps.org/supplemental/10.1103/PhysRevLett.130.113601, which includes Refs. [13,16,24,25,38,44,46–60], for additional technical considerations, pertaining to the method of regularized phase-space functions (including reconstruction techniques and relations to quantum coherence) and our generalized numeric toolbox, as well as experimental details.

[46] X. Ma, B. Berger, M. Aßmann, R. Driben, T. Meier, C. Schneider, S. Höfling, and S. Schumacher, Realization of all-optical vortex switching in exciton-polariton condensates, Nat. Commun. **11**, 897 (2020).
[47] J. Kasprzak, M. Richard, S. Kundermann, A. Baas, P. Jeambrun, J. M. J. Keeling, F. M. Marchetti, M. H. Szymánska, R. André, J. L. Staehli, V. Savona, P. B. Littlewood, B. Deveaud, and L. S. Dang, Bose-Einstein condensation of exciton polaritons, Nature (London) **443**, 409 (2006).
[48] W. P. Schleich, *Quantum Optics in Phase Space* (John Wiley & Sons, Berlin, 2001).
[49] J. Thewes, C. Lüders, and M. Aßmann, Conditional spectroscopy via nonstationary optical homodyne quantum state tomography, Phys. Rev. A **101**, 023824 (2020).
[50] M. Wouters and V. Savona, Stochastic classical field model for polariton condensates, Phys. Rev. B **79**, 165302 (2009).
[51] M. Wouters, I. Carusotto, and C. Ciuti, Spatial and spectral shape of inhomogeneous nonequilibrium exciton-polariton condensates, Phys. Rev. B **77**, 115340 (2008).
[52] W. Vogel and D.-G. Welsch, *Quantum Optics*, 3rd ed. (WileyVCH Verlag, Weinheim, 2006).
[53] T. Kiesel and W. Vogel, Universal nonclassicality witnesses for harmonic oscillators, Phys. Rev. A **85**, 062106 (2012).
[54] T. Kiesel and W. Vogel, Complete nonclassicality test with a photon-number-resolving detector, Phys. Rev. A **86**, 032119 (2012).
[55] E. Agudelo, J. Sperling, W. Vogel, S. Köhnke, M. Mraz, and B. Hage, Continuous sampling of the squeezed-state nonclassicality, Phys. Rev. A **92**, 033837 (2015).
[56] J. A. Hansen and C. Penland, Efficient approximate techniques for integrating stochastic differential equations, Mon. Weather Rev. **134**, 3006 (2006).
[57] R. Kumar, E. Barrios, A. MacRae, E. Cairns, E. H. Huntington, and A. I. Lvovsky, Versatile wideband balanced detector for quantum optical homodyne tomography, Opt. Commun. **285**, 5259 (2012).
[58] M. H. Szymańska, J. Keeling, and P. B. Littlewood, Mean-field theory and fluctuation spectrum of a pumped decaying Bose-Fermi system across the quantum condensation transition, Phys. Rev. B **75**, 195331 (2007).
[59] D. Caputo, D. Ballarini, G. Dagvadorj, C. Sánchez Muñoz, M. De Giorgi, L. Dominici, K. West, L. N. Pfeiffer, G. Gigli, F. P. Laussy, M. H. Szymańska, and D. Sanvitto, Topological order and thermal equilibrium in polariton condensates, Nat. Mater. **17**, 145 (2018).
[60] D. T. Smithey, M. Beck, J. Cooper, and M. G. Raymer, Measurement of number-phase uncertainty relations of optical fields, Phys. Rev. A **48**, 3159 (1993).
[61] N. I. Fisher, *Statistical Analysis of Circular Data* (Cambridge University Press, Cambridge, UK, 1993).
[62] J. Keeling, F. M. Marchetti, M. H. Szymańska, and P. B. Littlewood, Collective coherence in planar semiconductor microcavities, Semicond. Sci. Technol. **22**, R1 (2007).
[63] Note that, for our purpose, we define the threshold power not via a nonlinear increase of the total emission, but via the onset of quantum coherence in the specific mode filtered by the LO (cf. Ref. [45] for details). Thus, the threshold is meaningful for the mode that we actually measure and directly comparable to our simulation, being based on the same definition of P_{thr}.
[64] H. Sigurdsson, Hysteresis in linearly polarized nonresonantly driven exciton-polariton condensates, Phys. Rev. Res. **2**, 023323 (2020).
[65] E. Estrecho, M. Pieczarka, M. Wurdack, M. Steger, K. West, L. N. Pfeiffer, D. W. Snoke, A. G. Truscott, and E. A. Ostrovskaya, Low-Energy Collective Oscillations and Bogoliubov Sound in an Exciton-Polariton Condensate, Phys. Rev. Lett. **126**, 075301 (2021).
[66] S. Betzold, M. Dusel, O. Kyriienko, C. P. Dietrich, S. Klembt, J. Ohmer, U. Fischer, I. A. Shelykh, C. Schneider, and S. Höfling, Coherence and interaction in confined room-temperature polariton condensates with Frenkel excitons, ACS Photonics **7**, 284 (2020).
[67] I. Carusotto and C. Ciuti, Spontaneous microcavity-polariton coherence across the parametric threshold: Quantum Monte Carlo studies, Phys. Rev. B **72**, 125335 (2005).
[68] P. Comaron, G. Dagvadorj, A. Zamora, I. Carusotto, N. P. Proukakis, and M. H. Szymańska, Dynamical Critical Exponents in Driven-Dissipative Quantum Systems, Phys. Rev. Lett. **121**, 095302 (2018).
[69] R. Dall, M. D. Fraser, A. S. Desyatnikov, G. Li, S. Brodbeck, M. Kamp, C. Schneider, S. Höfling, and E. A. Ostrovskaya, Creation of Orbital Angular Momentum States with Chiral Polaritonic Lenses, Phys. Rev. Lett. **113**, 200404 (2014).
[70] E. Agudelo, J. Sperling, and W. Vogel, Quasiprobabilities for multipartite quantum correlations of light, Phys. Rev. A **87**, 033811 (2013).
[71] C. Flühmann and J. P. Home, Direct Characteristic-Function Tomography of Quantum States of the Trapped-Ion Motional Oscillator, Phys. Rev. Lett. **125**, 043602 (2020).
[72] T. Kiesel, W. Vogel, S. L. Christensen, J.-B. Béguin, J. Appel, and E. S. Polzik, Atomic nonclassicality quasiprobabilities, Phys. Rev. A **86**, 042108 (2012).